Micro ATR-FTIR spectroscopic imaging of atherosclerosis: an investigation of the contribution of inducible nitric oxide synthase to lesion composition in ApoE-null mice†

Francesca Palombo,[a] Hao Shen,[b] Lea Esther S. Benguigui,[b] Sergei G. Kazarian*[a] and Rita K. Upmacis*[b]

Inducible nitric oxide synthase (iNOS) has previously been shown to contribute to atherosclerotic lesion formation and protein nitration. Micro attenuated total reflection (ATR)-Fourier transform infrared (FTIR) spectroscopic imaging was applied *ex vivo* to analyse lesions in atherosclerotic (ApoE$^{-/-}$) mice. Histologies of cardiovascular tissue of ApoE$^{-/-}$ mice that contain the gene for iNOS and ApoE$^{-/-}$ mice without iNOS (ApoE$^{-/-}$iNOS$^{-/-}$ mice) were examined. Spectroscopic imaging of the aortic root revealed that iNOS did not affect the composition of the tunica media; furthermore, irrespective of iNOS presence, lipid esters were found to form the atherosclerotic plaque. ApoE$^{-/-}$ mouse aortic root lesions exhibited a more bulky atheroma that extended into the medial layer; signals characteristic of triglycerides and free fatty acids were apparent here. In ApoE$^{-/-}$iNOS$^{-/-}$ mouse specimens, lesions composed of free cholesterol were revealed. ATR-FTIR spectra of the intimal plaque from the two mouse strains showed higher lipid concentrations in ApoE$^{-/-}$ mice, indicating that iNOS contributes to lesion formation. The reduction of lesion prevalence in ApoE$^{-/-}$iNOS$^{-/-}$ mice compared with ApoE$^{-/-}$ mice is consistent with previous data. Moreover, the analysis of the plaque region revealed a change in the spectral position of the amide I band, which may be indicative of protein nitration in the ApoE$^{-/-}$ mouse, correlating with a more ordered (β-sheet) structure, while a less ordered structure was apparent for the ApoE$^{-/-}$iNOS$^{-/-}$ mouse, in which protein nitration is attenuated. These results indicate that micro ATR-FTIR spectroscopic imaging with high spatial resolution is a valuable tool for investigating differences in the structure and chemical composition of atherosclerotic lesions of ApoE$^{-/-}$ and ApoE$^{-/-}$iNOS$^{-/-}$ mice fed a high-fat Western diet and can therefore be applied successfully to the study of mouse models of atherosclerosis.

Introduction

Cardiovascular disease is a leading cause of death in the world. The underlying cause is atherosclerosis, which is recognized as an inflammatory disease.[1] Its pathogenesis involves a chronic response by the arterial wall that is promoted by macrophage migration, proliferation of smooth muscle cells and deposition of low density lipoproteins (LDLs), leading to plaque formation, heart attack and stroke.[2] Considering the contribution of this disease to morbidity and the fact that its prevalence is on the rise (due to an increased incidence of diabetes-related cardiovascular disease), there is a pressing need to improve medical diagnostic techniques, that not only identify the location of the plaque, but reveal information concerning the chemical identity of molecular constituents of the lesion.

In fact, biochemical changes taking place in the artery wall during atherogenesis may have a prominent effect on the clinical outcome of a plaque, the severity of which cannot be only established on the basis of morphological aspects. While ultrasound and magnetic resonance imaging (MRI) provide gross details about the lesion, other techniques, such as molecular imaging with either radionucleotides or affinity ligands, may only target highly specific sites.[3] Raman spectroscopy was used to characterize the chemical composition of normal and atherosclerotic human arterial walls, although sensitivity and spatial resolution in these pioneering studies was limited.[4–7] Nevertheless, Raman spectroscopy has a good potential for *in vivo* applications.[8] There are very recent advances in Raman spectroscopy, in particular with stimulated Raman scattering microscopy,[9] which promises exciting new developments in the biomedical field but it has not been applied yet to atherosclerosis. Infrared (IR) spectroscopy is particularly useful in biomedical applications.[10] IR spectroscopy was first employed in the study of atherosclerotic lesions in 1991, when Fourier transform-infrared (FTIR) microspectroscopy was applied to the analysis of molecular constituents of atherosclerotic arterial wall.[11] In recent years FTIR microspectroscopy has been enhanced by the use of focal plane array (FPA) infrared detectors that allowed simultaneous measurements of thousands of spectra from different locations within the sample, which is the basis of FTIR

[a] *Department of Chemical Engineering, Imperial College London, London, UK SW7 2AZ, UK. E-mail: s.kazarian@imperial.ac.uk; Tel: +44 (0)20 7594 5574*

[b] *Department of Pathology and Laboratory Medicine, Center of Vascular Biology, Weill Medical College of Cornell University, 1300 York Avenue, New York, NY 10065, USA. E-mail: rupmacis@med.cornell.edu; Tel: +1 (212) 746-6469*

† This paper is part of an *Analyst* themed issue on Optical Diagnosis. The issue includes work which was presented at SPEC 2008 Shedding Light on Disease: Optical Diagnosis for the New Millennium, which was held in São José dos Campos, São Paulo, Brazil, October 25–29, 2008.

spectroscopic imaging. FTIR imaging of biomedical samples is a rapidly developing area with applications ranging from organs, such as skin,[12] bone[13] or brain,[14,15] to vasculature,[16–18] cancerous tissues,[19,20] the use of murine embryonic stem cells in tissue engineering,[21] dried[22] or live cancer cells.[23] Conventional FTIR spectroscopy using the attenuated total reflection (ATR) approach has been used for characterization of atherosclerotic rabbit aorta.[24,25] FTIR imaging using an ATR microscope objective with germanium crystal (refractive index = 4) was applied to observe structures within atherosclerotic rabbit aorta with high spatial resolution (3–4 μm).[26] Macro ATR-FTIR spectroscopic imaging is a powerful tool for analysing hydrated biological tissues or samples in contact with water.[27]

The application of micro ATR-FTIR imaging to *ex vivo* biomedical specimens enables compositional information to be obtained as well as the spatial distribution of different constituents of the tissue with a high spatial resolution. In a recent work, the capability of micro ATR-FTIR spectroscopic imaging to detect changes in the structure and chemical composition of atherosclerotic lesions in the thoracic aorta near intercostal branch ostia of immature and mature rabbits fed cholesterol with or without L-arginine supplements has been demonstrated.[28]

Although a multitude of factors contribute to atherogenesis, the discovery of nitric oxide (NO) as a potent vasodilator, other than a poisonous gas and toxic air pollutant, has been important in the investigation of physiological processes that maintain vascular homeostasis. NO is produced by a family of NO synthase (NOS) enzymes: endothelial, neuronal and inducible NOS (eNOS, nNOS and iNOS, respectively; or NOS3, NOS1 and NOS2, respectively). All NOS isoforms are dimers requiring several cofactors: heme, flavin adenine dinucleotide (FAD), flavin mononucleotide (FMN), tetrahydrobiopterin (BH$_4$), calmodulin and zinc.[29] During NOS activity, O$_2$ and arginine are metabolized and NO radicals released. Notably, O$_2$ consumption must be tightly coupled to e$^-$ transfer during catalysis, otherwise NOS switches from producing NO to releasing superoxide radical anion (O$_2^{\bullet-}$), a reactive oxygen species.[30–32] While eNOS is constitutively expressed in the endothelium under normal conditions, nNOS and iNOS are either at low levels or non-detectable.[33] However, during atherosclerosis, all three forms of NOS are detectable, with eNOS and nNOS both providing an anti-atherogenic function,[34,35] while iNOS is inflammatory, producing larger amounts of NO than either eNOS or nNOS and promoting disease.[36–38] Paradoxically, despite the presence of all NOS isoforms, NO bioavailability is reduced during atherosclerosis.[39] In human atherosclerotic lesions, iNOS has been localized in macrophages, foam cells and vascular smooth muscle cells.[40] iNOS also co-localizes with proteins in the lesion in which tyrosine residues are nitrated in one of the symmetric *ortho*-positions of the phenyl ring, indicating that iNOS plays a role in protein 3-nitrotyrosine formation (henceforth denoted as protein nitration).[41,42] Thus, while the basis for the opposing roles of NOS isoforms in atherogenesis may not be fully known, iNOS may contribute to disease progression by increasing oxidative stress. In this regard, high NO levels generated by iNOS may couple with O$_2^{\bullet-}$, also increased during atherosclerosis,[43] to produce peroxynitrite (ONOO$^-$) with resultant protein nitration. Indeed, extensive protein nitration is observed during atherosclerosis, as well as during many disease states.[40,44]

Mouse models of atherosclerosis that represent several aspects of the human condition have proved to be extremely useful in exploring molecular mechanisms involved in the progression of this disease. Normal mice do not develop atherosclerosis, but with the deletion of the apolipoprotein E gene (denoted as ApoE$^{-/-}$), mice rapidly develop aortic lesions.[45] The ApoE amphipathic protein plays a pivotal role in lipoprotein trafficking by acting as a ligand for the receptor-mediated clearance of cholesterol and triglyceride-rich lipoprotein constituents.[46] The normotensive ApoE$^{-/-}$ mice exhibit plasma cholesterol levels 4–5 times greater than wild-type mice and spontaneously develop atherosclerotic lesions,[45] although this condition is exacerbated when these mice are fed a high-fat 'Western diet'.[47]

To determine the contribution of iNOS to atherogenesis, ApoE$^{-/-}$ mice were engineered to also contain a deletion of the iNOS gene (denoted as ApoE$^{-/-}$iNOS$^{-/-}$ mice).[34,36–38] When fed a normal chow diet, these mice developed atherosclerotic lesions that were indistinguishable in size to those from ApoE$^{-/-}$ mice, leading to the initial view that iNOS-derived species do not contribute to atherogenesis.[34] However, on feeding these mice a Western diet to accelerate lesion development, genetic deficiency of iNOS decreased atherosclerosis in ApoE$^{-/-}$iNOS$^{-/-}$ mice.[36–38] In fact, it was demonstrated that after 24 weeks of a Western diet, the aortic lesion area was reduced by 38% and 40% in male and female mice, respectively.[37] Thus, iNOS accelerates lesion progression during atherogenesis. Using these mice, it was demonstrated that iNOS contributes to protein nitration in the atherosclerotic lesion, as well as in other organs distal to the aortic plaque.[48,49]

In this study, we used micro ATR-FTIR spectroscopic imaging to probe whether differences can be seen in the chemical composition of the blood vessel wall and atherosclerotic lesion in the aortic root of ApoE$^{-/-}$ and ApoE$^{-/-}$iNOS$^{-/-}$ mice fed a high-fat Western diet for 24 weeks. In particular, we sought to determine whether evidence of protein nitration, prevalent in ApoE$^{-/-}$ mice, but diminished in ApoE$^{-/-}$iNOS$^{-/-}$ mice, could be obtained by micro ATR-FTIR imaging.

Materials and methods

Animals

The animal procedures applied in this study complied with the Weill Medical College of Cornell University Care and Use Committee. Mice missing both ApoE and iNOS genes (designated as ApoE$^{-/-}$iNOS$^{-/-}$ mice) were originally obtained from Dr N. Maeda (University of North Carolina at Chapel Hill) and were derived from at least 6 generations of backcross breeding to C57BL/6J mice.[34] ApoE$^{-/-}$iNOS$^{-/+}$ heterozygote mice were bred to generate both ApoE$^{-/-}$iNOS$^{+/+}$ (designated as ApoE$^{-/-}$) and ApoE$^{-/-}$iNOS$^{-/-}$ mice as littermates. The animals were genotyped as previously described.[48,49] ApoE$^{-/-}$iNOS$^{-/-}$ mice were studied as the experimental group, while ApoE$^{-/-}$ mice served as control. Three male mice per group were analysed, giving a total of 6 mice. They were weaned at three weeks of age and then fed a Western diet comprising (w/w) 21.2% anhydrous milk fat, 17.3% protein, 48.5% carbohydrate, and a total of 0.2% cholesterol (Harlan Teklad; TD 88137) for 24 weeks. More specifically, the diet contains a mix of fatty acids (FAs): saturated FAs (13.3% of calories in the diet), monounsaturated FAs (MUFAs; 5.9%)

and polyunsaturated FAs (PUFAs; 0.9%). The FAs that are present in higher levels in the diet include: myristic (tetradecanoic), palmitic (hexadecanoic) and stearic (octadecanoic) acids, which are saturated FAs and represent 10.3%, 29.4% and 12.6% of the total FAs present, respectively; oleic acid and isomers (20.7% and 4.7% of the total FAs present, respectively) represent the major MUFAs; and linoleic and linolenic acids represent the PUFAs (2.3% and 0.6% of the total FAs). Eicosapentaenoic acid and docosahexaenoic acid combined represent <0.5% of the total FAs.
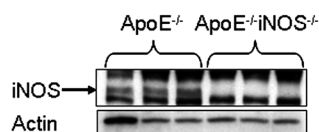
At 27 weeks of age they were euthanized, and the heart and aortic root retained for this study. There were no significant differences in the body weights of the Western diet-fed ApoE$^{-/-}$ versus ApoE$^{-/-}$iNOS$^{-/-}$ male mice prior to euthanasia.[36,37,48,49]

Sample preparation

Following euthanasia, the hearts were surgically removed with a small amount of the aorta attached, rinsed with phosphate buffered saline (PBS) and cryopreserved in a mixture of OCT (Optimal Cutting Temperature compound; Sakura Finetek) and sucrose (30%; in deionized water) in a 1 : 1 ratio using an isopentane/liquid nitrogen bath. Serial frozen sections (8 μm thickness) were obtained by cryostat sectioning in the region of the aortic leaflet and mounted onto glass slides. The glass slides were washed in PBS (30 min) to remove the embedding compound and air dried (24 hours) prior to analysis.

Western blotting of homogenized hearts from ApoE$^{-/-}$ and ApoE$^{-/-}$iNOS$^{-/-}$ mice

In order to determine the presence of iNOS in the tissue samples, hearts from ApoE$^{-/-}$ and ApoE$^{-/-}$iNOS$^{-/-}$ mice ($n = 3$) fed a Western diet for 24 weeks were homogenized, probed and visualized for iNOS at ~130 kDa (polyclonal rabbit iNOS antibody; Santa Cruz, sc-560) and for actin at ~43 kDa (polyclonal goat actin antibody; Santa Cruz, sc-1615) in a manner described previously.[48,49] Fig. 1 demonstrates that iNOS is present in hearts from ApoE$^{-/-}$ (indicated by an arrow), but absent in ApoE$^{-/-}$iNOS$^{-/-}$ mice. Of several iNOS antibodies tested in this application, the best antibody (with regard to reproducible iNOS detection) also resulted in the appearance of non-specific bands at higher and lower molecular weights than iNOS, an effect that has also been reported previously.[50,51] We have previously documented that iNOS is present in aortae from ApoE$^{-/-}$ mice, but is missing in ApoE$^{-/-}$iNOS$^{-/-}$ mice.[49]

Fig. 1 Heart tissue from ApoE$^{-/-}$ mice containing iNOS ($n = 3$) or without iNOS (ApoE$^{-/-}$iNOS$^{-/-}$; $n = 3$) was analysed for protein iNOS and actin expression by Western blotting. The presence of iNOS is indicated by an arrow, and bands above and below are the result of non-specific binding of the antibody, noted by others previously.[50,51] The mice were subjected to a Western diet for 6 months. Each band represents tissue from a single mouse.

FTIR spectroscopic imaging

Six aortic root sections per animal (6 mice) were analysed, giving a total of 36 specimens. Two measurements per section were collected, at different locations within the tissues, to obtain a relevant number of imaging datasets of these samples (72 spectroscopic images).
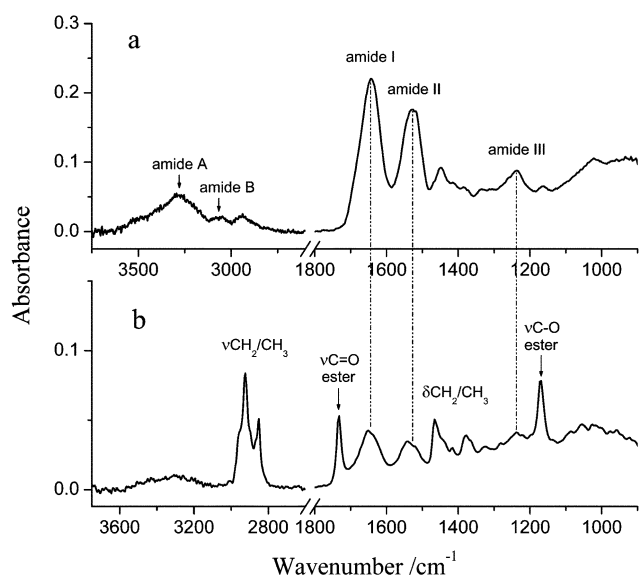
Micro ATR-FTIR images were acquired using a rapid scan system, with a Bio-Rad FTS-60A spectrometer coupled to a Varian (model 600 UMA) IR microscope, and a liquid nitrogen-cooled focal plane array (FPA) detector. A Varian slide-on ATR accessory with germanium crystal (Refractive Index = 4; Numerical Aperture = 2.4) was attached to a 15× Cassegrain objective mounted on the IR microscope. The use of a germanium crystal allows a spatial resolution of about 3–4 μm to be achieved in the fingerprint region of the mid-infrared spectrum.[26] The detector consisted of 4096 pixels (size 40 μm × 40 μm each), arranged in a 64 × 64 array, giving an image over a 63 μm × 63 μm area of the specimen. Prior to the measurement, a visible image of the section was recorded using the 15× objective on the IR microscope with its reflection mode coupled to the FPA detector. No ATR correction was applied to the measured FTIR spectra before analysis.

During the time of measurement, the crystal was brought into contact with the surface of the sample for the analysis. For soft materials such as the histologies used in this study, a low contact pressure generally ensures a good signal-to-noise ratio of the spectra without damaging the sample. The evanescent wave has a depth of penetration of 1.2 μm at a wavenumber of 1000 cm^{-1} ($\lambda = 10$ μm) here.

Accurate positioning and focus adjustment of the ATR accessory were performed before each series of measurements. An FTIR image was obtained by simultaneous acquisition of 4096 spectra from the pixels of the array detector. Each pixel measures an IR absorption spectrum at a specific location within the sample. The spectra were acquired over the range 4000–900 cm^{-1} at 4 cm^{-1} resolution and 2 zero-filling factor, by co-addition of 256 interferograms. An image in the absence of a sample (background) was collected before each measurement. Varian Resolution Pro 4.0 software was used for acquisition and manipulation of the spectral datasets.

Each image is a hyperspectral data cube having two spatial dimensions and one dimension given by the spectral coordinate (i.e. wavenumber); values in each dataset are absorbances at various combinations of position and wavenumber. Absorbance of IR bands provides quantitative information about a particular chemical component. The fingerprint region of the mid-IR spectrum between 1800 and 900 cm^{-1}, containing the signatures of proteins and lipids in the aortic tissues, was selected for the analysis. Band absorbance was assessed by integration method, with a linear baseline drawn through the peak edges, and the spectrum above this line integrated over the wavenumber range of the band.

Fig. 2 shows typical ATR-FTIR spectra of medial lamellae and atherosclerotic plaque from aortic root specimens of ApoE$^{-/-}$iNOS$^{-/-}$ and ApoE$^{-/-}$ mice, respectively. (They are individual profiles extracted from specific regions within micro ATR-FTIR images of those samples.) Signals of proteins, which are the main constituents of the vascular tissue, were identified in

Fig. 2 Typical ATR-FTIR spectra of (a) medial lamellae and (b) atherosclerotic lesion extracted from micro ATR-FTIR images of aortic root cross-sections of ApoE$^{-/-}$iNOS$^{-/-}$ and ApoE$^{-/-}$ mice, respectively.

both these profiles: in particular, two prominent bands in the ranges 1720–1585 cm^{-1} and 1585–1481 cm^{-1} originating from the C=O stretching and N–H bending (coupled to a C–N stretching) of the peptide group and referred to as amide I and II, respectively; a band at about 1238 cm^{-1}, attributed to the C–H bending of the same functional group and termed amide III. The amide A and B bands at 3290 and 3060 cm^{-1}, respectively, associated with the N–H bond of the peptide group, were also recognized in the spectrum of the lamellae. Characteristic signals due to the lipids were detected in the spectrum of the plaque: the strong, narrow band at 1733 cm^{-1}, due to the C=O stretching mode of lipid esters (mainly cholesteryl esters[52]); two major absorptions at 2924 and 2852 cm^{-1}, assigned to the asymmetric and symmetric stretching vibrations of lipid acyl CH$_2$ groups, respectively. (Minor contribution to the CH-stretching pattern in the range 3000–2800 cm^{-1} arises from CH$_3$ groups of both lipids and

proteins.) Other major features are the scissoring vibrations of CH$_2$ and CH$_3$ groups, giving rise to the bands at 1464 and 1380 cm^{-1} respectively, and the ester C–O stretching signal at 1171 cm^{-1}, which is typical of lipid esters. (For the assignment of the spectral features see Parker[53] and Ahmed et al.[54])
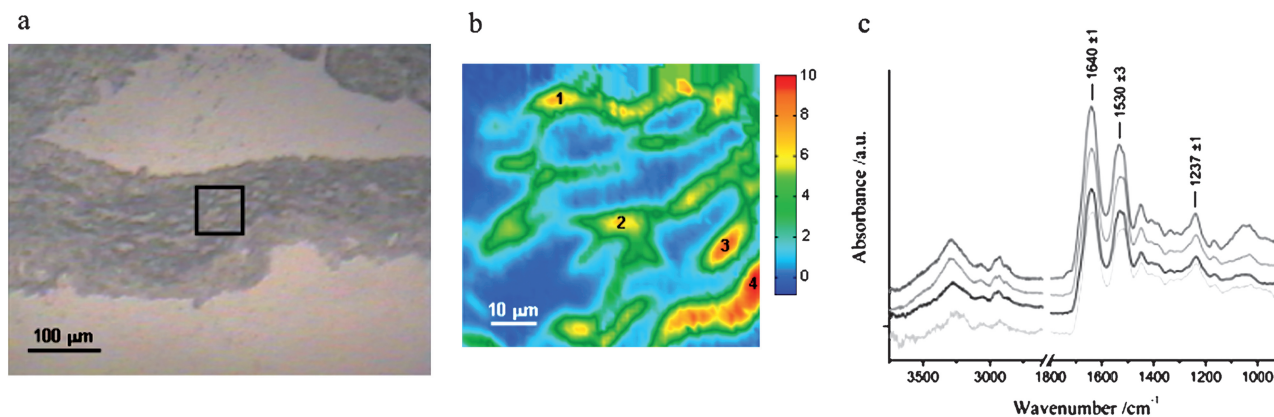
Based on the integrated absorbance of a particular band of the mid-IR spectrum (generally in the fingerprint region below 1800 cm^{-1}), spectroscopic images could be obtained depicting the distribution of corresponding chemical species within a specimen. Micro ATR-FTIR images representing the concentration maps for proteins and lipids within the aortic root tissue at different locations were obtained by integration of the amide I and ν(C=O)$_{ester}$ absorption bands, respectively. (Water absorption may create a problem of overlap with amide bands; however, the specimens used in this study are aortic root cryosections cut from frozen material and air dried, thus without water.) ISys 4.0 data analysis software (Spectral Dimensions Inc., Maryland, US) was used to obtain average FTIR profiles for selected (2 × 2-pixel) regions of the images, and to create composite two-color images representing the compositional map of a sample at a given location.
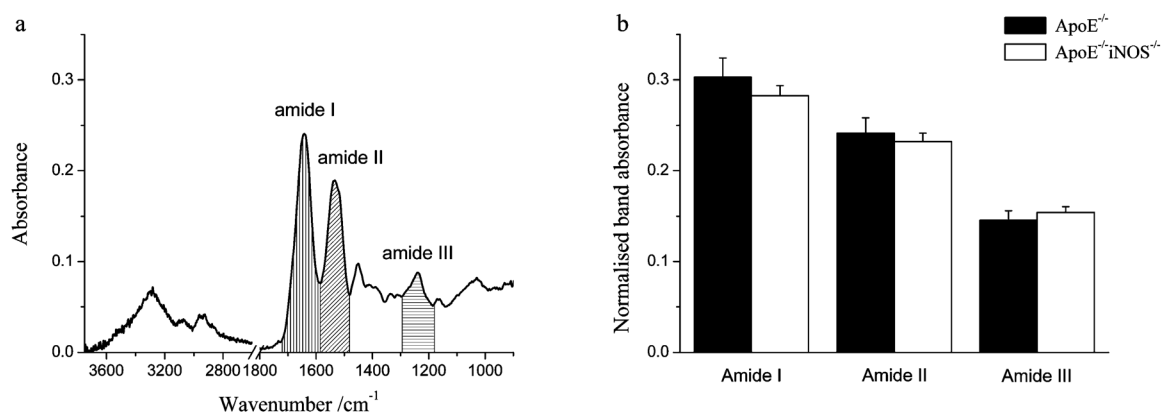
Results

Ex vivo analysis of 36 cross-sections of aortic root from ApoE$^{-/-}$ and ApoE$^{-/-}$iNOS$^{-/-}$ mice was carried out by micro ATR-FTIR spectroscopic imaging. Tissues were examined at different locations of the aortic wall in order to characterize their structure and chemical composition.

Medial lamellae

Fig. 3a is a visible image of a cross-section of aortic root from an ApoE$^{-/-}$ mouse fed a high-fat Western diet; the square indicates the location within the tunica media from which a micro ATR-FTIR imaging measurement was acquired. The image in Fig. 3b is the univariate distribution of integrated absorbance for the amide I band, in the range 1720–1585 cm^{-1}, across the detector array. Lamellar motifs typical of the medial structure[55] are nicely depicted here. Average profiles, each calculated from 4 individual

Fig. 3 (a) Photomicrograph (15× magnification) of a cross-section of ApoE$^{-/-}$ mouse aortic root; the square indicates the location from which the FTIR image was obtained. (b) Micro ATR-FTIR image (63 µm × 63 µm size) obtained *via* integration of the amide I band, in the range 1720–1585 cm^{-1}; numbers indicate the regions from which average spectra were obtained. (c) Average profiles obtained from 2 × 2-pixel regions within the image; vibrational frequencies (mean ± shift) of amide I, II and III are presented.
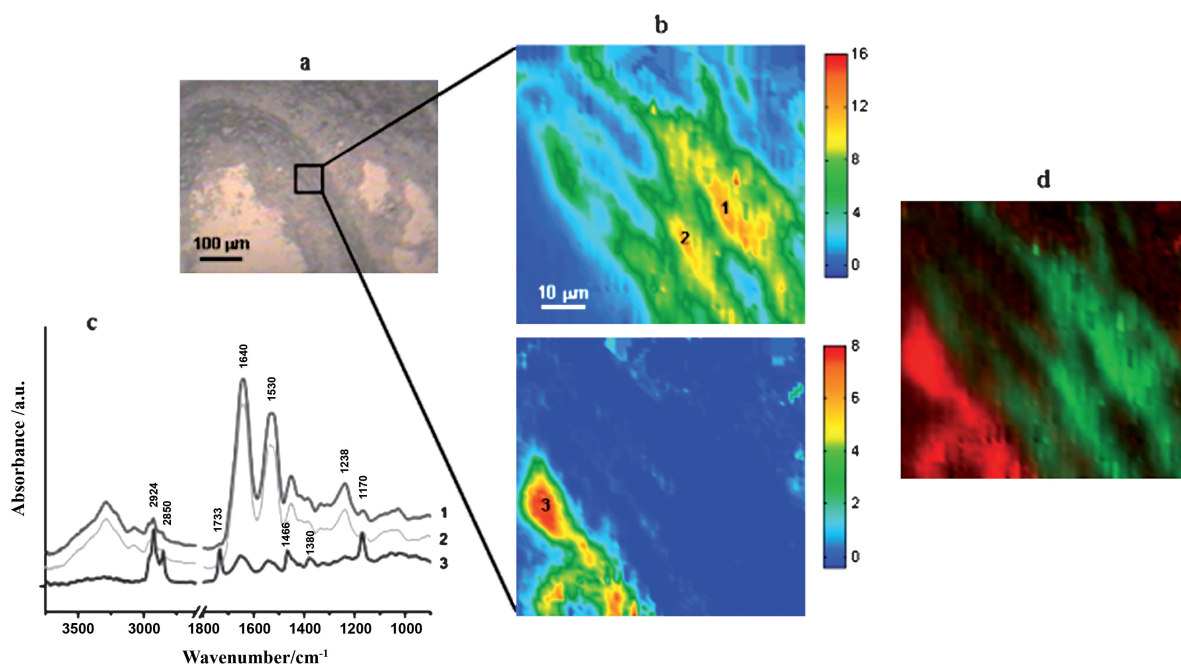
Fig. 4 Average profiles (from 2 × 2-pixel regions) were obtained from FTIR images of the medial layer in different specimens (one section per animal). (a) Absorbance of the three main peptide bands was assessed by integration over the ranges of 1720–1585 (amide I), 1585–1481 (amide II), 1294–1186 cm^{-1} (amide III) without baseline correction; each value was then normalised with respect to the absorbance of the entire fingerprint spectrum, 1800–1140 cm^{-1} (no baseline applied). This represents the relative contribution of the peptide bands in the spectra of lamellae for ApoE$^{-/-}$ and ApoE$^{-/-}$iNOS$^{-/-}$ mice. (b) The data are the means for each group.

spectra (2 × 2-pixels) and representing a given lamella of the image above, are shown in Fig. 3c. The main absorption features here are due to the amide I, II and III vibrations (at 1640, 1530 and 1237 cm^{-1}) of the structural proteins elastin and collagen, which are the major components of the aortic media.[56] The average spectra are very similar to each other with respect to the absorption intensity and peak position of the peptide bands, indicating a homogeneous composition of elastic lamellae within the tissue. Furthermore, average profiles obtained from the FTIR images of the tunica media in the different specimens showed very little variation from one to another. All three

peptide bands have similar absorbance in ApoE$^{-/-}$ mice compared with ApoE$^{-/-}$iNOS$^{-/-}$ mice (Fig. 4b; Fig. 4a shows the integration method applied to the three peptide bands). These results indicate that the composition of the tunica media is very consistent within and between aortic root specimens.

Intimal plaque

Fig. 5a shows a photomicrograph of a cross-section of ApoE$^{-/-}$ mice aortic root. Micro ATR-FTIR images from a location of the intima-medial layer are presented in Fig. 5b. Each image
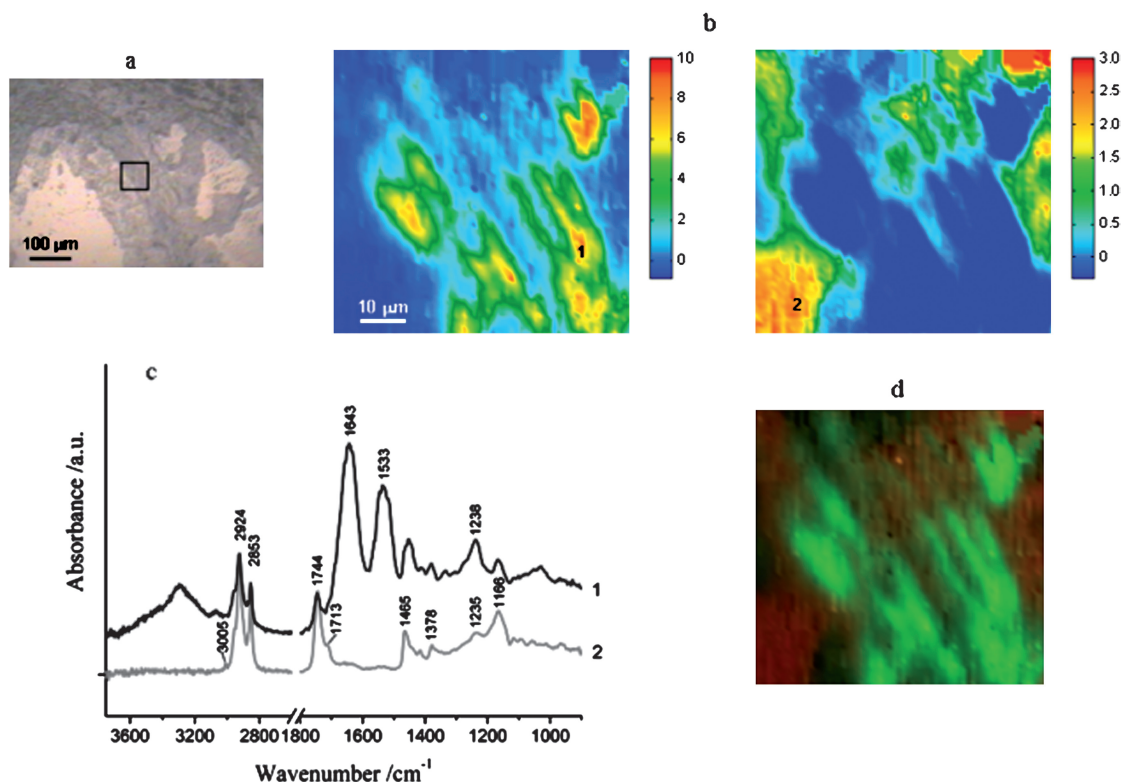

Fig. 5 (a) Photomicrograph (15× magnification) of a cross-section of ApoE$^{-/-}$ mouse aortic root; the square indicates the location from which the FTIR images were obtained. (b) Micro ATR-FTIR images (each of 63 µm × 63 µm size) obtained *via* integration of (top) amide I band, 1705–1585 cm^{-1}, and (bottom) ν(C=O)$_{ester}$ signal, 1760–1705 cm^{-1}; numbers indicate the regions from which average spectra were obtained. (c) Average profiles calculated from 2 × 2-pixel regions within the images. (d) Two-color composite image of the ApoE$^{-/-}$ mouse aortic root section obtained by overlying the FTIR images of lamellae (green) and plaque (red).

represents the distribution of integrated absorbance of a different band of the mid-IR spectrum for each pixel of the FPA detector. Lamellar-like structures are visible in the image derived from integration of the amide I band, in the range 1705–1585 cm^{-1} (Fig. 5b; top). An atherosclerotic lesion is also revealed at this location of the tissue through the distribution of the integrated absorbance of the ν(C=O)$_{ester}$ band, in the range 1760–1705 cm^{-1} (Fig. 5b; bottom). Representative profiles for the structures depicted in these images are displayed in Fig. 5c. The two spectra of the lamellae are very similar to one another, and to those extracted from the image of tunica media above (see Fig. 3c). On the other hand, the spectrum of the plaque contains typical features of lipid esters, namely the ν(C=O) band at 1733 cm^{-1} and the ν(C–O) signal at 1170 cm^{-1}. In the plaque, lipid esters (essentially cholesteryl esters) are aggregated forming hydrophobic clusters; the presence of peptide bands in the spectrum of the lesion may reflect the formation of macrophage-derived foam cells, as already reported for a rabbit model of the disease.[26,28] Images of the lamellae and plaque derived from the same measurement (Fig. 5b) are complementary, as shown by the composite image in Fig. 5d.
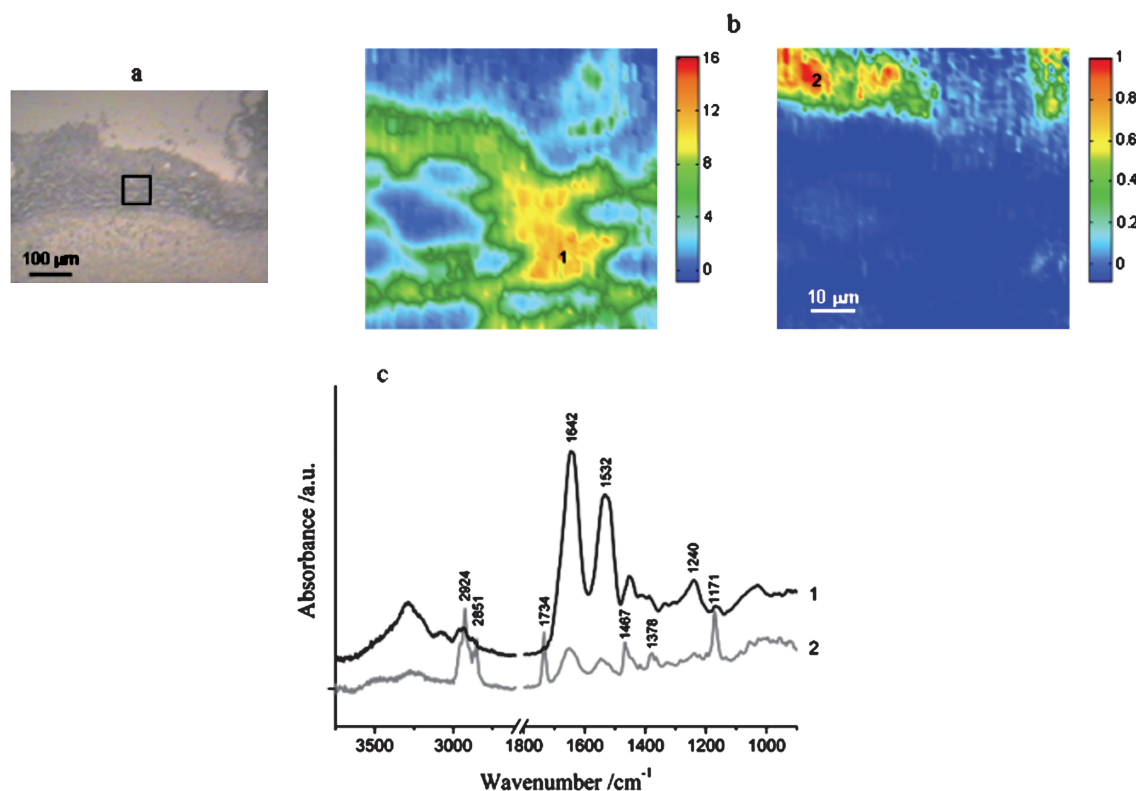
Lesions with a bulky atheroma made of triglycerides and fatty acids were revealed in the case of ApoE$^{-/-}$ mice samples but not in the ApoE$^{-/-}$iNOS$^{-/-}$ mice samples upon analysing small portions of intimal tissue. Fig. 6 shows the visible and spectroscopic images for a micro ATR-FTIR imaging measurement

collected at the intima-medial layer of an ApoE$^{-/-}$ mouse specimen. Absorption signals in the spectrum of the lesion (see profile 2 in Fig. 6c) originate from esterified and free fatty acids; in particular, the signal at 1744 cm^{-1} is associated with the C=O stretching mode of the ester group in triglycerides (and other esterified fatty acids), whereas the shoulder at 1713 cm^{-1} is due to the C=O stretching mode of free fatty acids.[57] (Note the close resemblance of this profile with the spectrum of an oil containing a high amount of erucic acid, reported by Ahmed *et al.*[54] Furthermore, similar peak positions for esterified and free fatty acids have been reported for human mucosal tissue by Yoshida *et al.*[58]) A minor absorption at 3005 cm^{-1} can be related to the olefinic =CH stretching of unsaturated lipids.[59]

In ApoE$^{-/-}$iNOS$^{-/-}$ mice, the presence of lipid deposits giving rise to atherosclerotic plaques was also evidenced. Fig. 7 shows visible and spectroscopic images of a region of the intima-medial layer within an aortic root cross-section of ApoE$^{-/-}$iNOS$^{-/-}$ mice. A plaque lying above the lamellar structure of the media is depicted here (Fig. 7b); the corresponding spectrum (profile 2 in Fig. 7c) contains typical features of lipid esters already evidenced for the plaque in the ApoE$^{-/-}$ mouse sample. (Note the similarities between this spectrum and the profile 3 in Fig. 5c.) These data indicate a similar biochemical composition of plaque in ApoE$^{-/-}$ and ApoE$^{-/-}$iNOS$^{-/-}$ mice aortic roots. Lesions composed of free (unesterified) cholesterol were also revealed in ApoE$^{-/-}$iNOS$^{-/-}$ mice specimens, as shown in Fig. 8. In this case,

Fig. 6 (a) Photomicrograph (15× magnification) of a cross-section of ApoE$^{-/-}$ mouse aortic root; the square indicates the location from which the FTIR images were obtained. (b) Micro ATR-FTIR images (each of 63 μm × 63 μm size) obtained *via* integration of (left) amide I band, 1705–1585 cm^{-1}, and (right) ν(C=O)$_{ester}$ signal, 1780–1670 cm^{-1}; numbers indicate the regions from which average spectra were obtained. (c) Average profiles calculated from 2 × 2-pixel regions within the images. (d) Two-color composite image of the ApoE$^{-/-}$ mouse aortic root section obtained by overlying the FTIR images of lamellae (green) and plaque (red).

Fig. 7 (a) Photomicrograph (15× magnification) of a cross-section of ApoE$^{-/-}$iNOS$^{-/-}$ mouse aortic root; the square indicates the location from which the FTIR images were obtained. (b) Micro ATR-FTIR images (each of 63 μm × 63 μm size) obtained *via* integration of (left) amide I band, 1705–1585 cm^{-1}, and (right) ν(C=O)$_{ester}$ signal, 1760–1705 cm^{-1}; numbers indicate the regions from which average spectra were obtained. (c) Average profiles calculated from 2 × 2-pixel regions within the images.
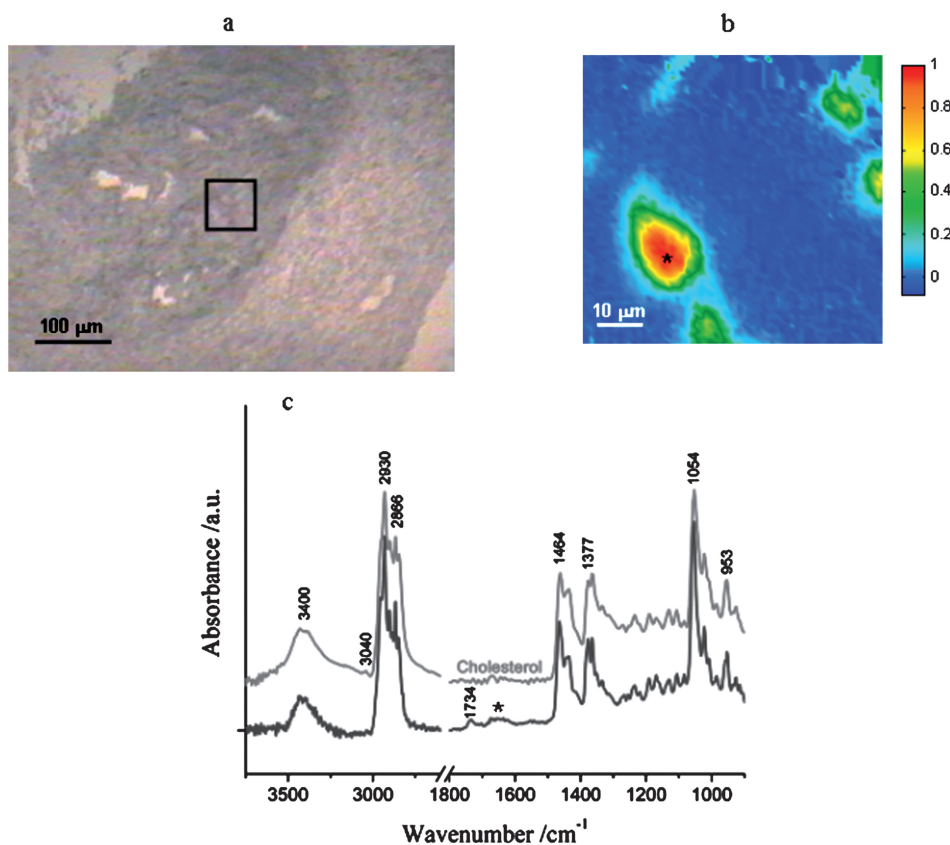
cholesterol molecules are associated forming aggregates distributed within the intima-medial region of the aortic root tissue (Fig. 8b). Mid-IR spectral features related to these largely hydrophobic entities reproduce the characteristic signals of pure cholesterol (Sigma-Aldrich, purity >99 wt%) (Fig. 8c); in particular, the bands at 3400 cm^{-1} (bonded O–H stretching), 3040 cm^{-1} (aromatic C–H stretching of the sterol ring), 2930 and 2866 cm^{-1} (>CH$_2$ asymmetric and symmetric stretching, respectively), 1464 and 1377 cm^{-1} (>CH$_2$ and –CH$_3$ bending, respectively), 1054 and 953 cm^{-1} (C–C backbone stretching vibrations) were recognized here.[60–62] Additionally, the spectrum of the lesion presents the signal at 1734 cm^{-1} due to the ester carbonyl stretching of cholesterol derivatives (cholesteryl esters).

Plaque composition and nitrated proteins

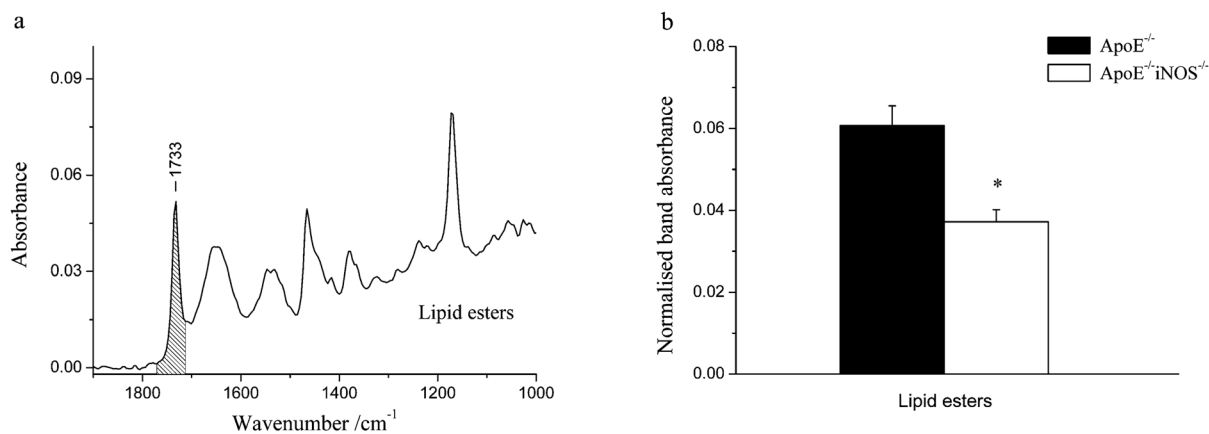Fig. 9 shows the results of plaque analysis applied to the micro ATR-FTIR images of ApoE$^{-/-}$ and ApoE$^{-/-}$iNOS$^{-/-}$ mice aortic root. FTIR average profiles from 2 × 2-pixel regions were compared for both mouse strains and the C=O stretching band representing lipid esters (1733 cm^{-1}, Fig. 9a) was examined. Fig. 9b provides average integrated absorbance (related to analyte concentration) of this lipid band and shows that significantly lower lipid ester levels were found in plaques from ApoE$^{-/-}$iNOS$^{-/-}$ mice compared to ApoE$^{-/-}$ mice. These results indicate that iNOS contributes to lipid accumulation in the atherosclerotic plaque, consistent with previous findings.[36]

Fig. 10 shows ATR-FTIR spectra of atherosclerotic plaques extracted from spectroscopic images of ApoE$^{-/-}$ and ApoE$^{-/-}$iNOS$^{-/-}$ mice aortic root samples. Both profiles were normalised with respect to the absorbance of the amide I band, in the range 1705–1585 cm^{-1}. The spectrum of the ApoE$^{-/-}$ mouse sample presents the strongest absorbance of the lipid bands (namely C–H and C=O stretching signals), indicating a higher lipid concentration of lesion in ApoE$^{-/-}$ mouse compared with ApoE$^{-/-}$iNOS$^{-/-}$ mouse. The reduction of lesion prevalence in ApoE$^{-/-}$iNOS$^{-/-}$ mice compared with ApoE$^{-/-}$ mice is consistent with quantitative data on intimal lesion area obtained by tracing and quantifying stained aortic root sections.[36–38]

Analysis of the peak position of the ν(C=O)$_{ester}$ band, in the range 1780–1700 cm^{-1}, reveals the presence of esterified fatty acids and triglycerides in the ApoE$^{-/-}$ mouse sample (peak maximum at 1744 cm^{-1}), whereas cholesteryl esters are abundant in the ApoE$^{-/-}$iNOS$^{-/-}$ mouse sample (peak maximum at 1733 cm^{-1}) (Fig. 10b). Also, a change in the peak position of the amide I band is clearly revealed here, the ApoE$^{-/-}$ mouse spectrum showing a maximum at 1632 cm^{-1}, which is shifted at 1653 cm^{-1} in the ApoE$^{-/-}$iNOS$^{-/-}$ mouse spectrum. This spectral effect may be attributed to a change in the secondary structure for the proteins in the region of the lesion between the two groups of animals. A lower wavenumber position of the amide I band maximum in the ApoE$^{-/-}$ mouse profile may correlate with an increase of (β-sheet) ordered structure for the proteins in the lesion area, while less ordered peptide structures would

Fig. 8 (a) Photomicrograph (15× magnification) of a cross-section of ApoE$^{-/-}$iNOS$^{-/-}$ mouse aortic root; the square indicates the location from which the FTIR image was obtained. (b) Micro ATR-FTIR image (63 μm × 63 μm size) obtained *via* integration of the C–C stretching band, in the range 1075–1030 cm^{-1}; the star indicates the region from which an average spectrum was obtained. (c) Average profile obtained from a 2 × 2-pixel region within the image; the FTIR spectrum of pure cholesterol (Sigma-Aldrich, purity >99 wt%) is also shown.

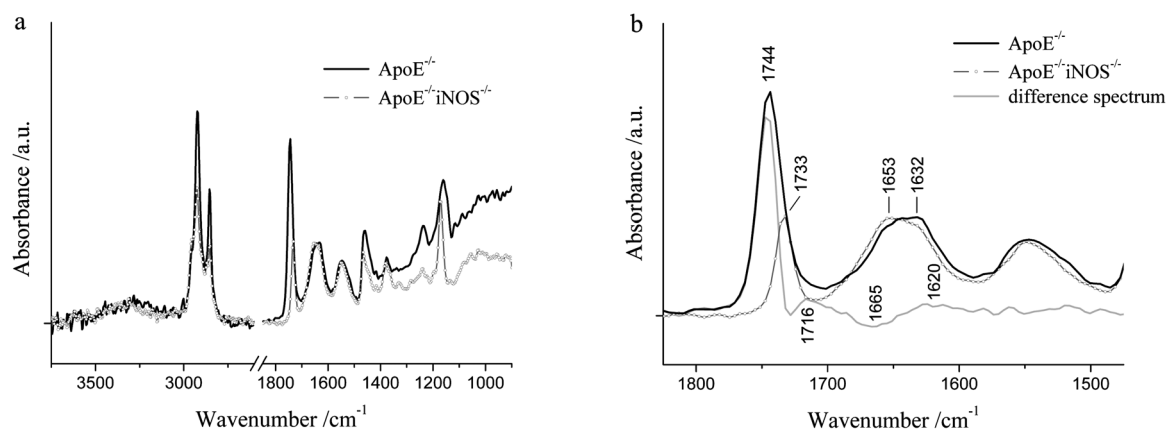
Fig. 9 Average profiles (from 2 × 2-pixel regions) were obtained from FTIR images of the intimal plaque in different specimens (one section per animal). (a) Absorbance of the lipid ester C=O stretching band was assessed by integration over the range of 1771–1713 cm^{-1} without baseline correction (see shown ApoE$^{-/-}$ mice spectrum); each value was then normalised with respect to the absorbance of the entire fingerprint spectrum, 1800–1140 cm^{-1} (no baseline applied). This represents the relative contribution of the lipid ester band in the spectra of the lesion for ApoE$^{-/-}$ and ApoE$^{-/-}$iNOS$^{-/-}$ mice. (b) The data are the means for each group; *, $p < 0.05$.

characterize the ApoE$^{-/-}$iNOS$^{-/-}$ mouse. Such an effect has been previously evidenced for a specific protein, α-synuclein, and attributed to the nitration of the peptide.[63] Here the depletion of absorbance at *ca.* 1665 cm^{-1} (disordered conformation)

accompanied by an enhancement at *ca.* 1620 cm^{-1} (ordered conformation), evidenced by the difference spectrum in Fig. 10b (note that the position of resultant bands after subtraction may slightly shift), can be also referred to as an effect of protein

Fig. 10 (a) Representative FTIR spectra of the lesion extracted from micro ATR-FTIR images of ApoE$^{-/-}$ and ApoE$^{-/-}$iNOS$^{-/-}$ mice aortic root samples and normalised with respect to the amide I band peak absorbance. (b) Expanded spectral region showing the C=O stretching, amide I and amide II bands. A difference spectrum was obtained by subtracting the ApoE$^{-/-}$ iNOS$^{-/-}$ profile from the ApoE$^{-/-}$ profile; it shows a loss of absorbance for the ApoE$^{-/-}$ spectrum at *ca.* 1665 cm^{-1} and a gain at *ca.* 1620 cm^{-1}. The amide I subcomponents associated with these spectral positions can be assigned to the vibrations of α-helical (1665 cm^{-1}) and β-sheet (1620) structures of the peptide.[64]

nitration in the ApoE$^{-/-}$ mouse sample. (The parallel mode of the β-sheet structure representing an ordered conformation is at 1620 cm^{-1}.[64]) The typically disordered structure, observed in the absence of nitration, is instead revealed for the ApoE$^{-/-}$iNOS$^{-/-}$ mouse sample.

Discussion

In this study, micro ATR-FTIR spectroscopy was applied as a local probe with chemical specificity and high spatial resolution to the study of different point locations of aortic root sections from atherosclerotic ApoE$^{-/-}$ and ApoE$^{-/-}$iNOS$^{-/-}$ mice fed a high-fat Western diet for 6 months. A comparison of data collected for these two strains of mice highlighted similarities and differences in the structure and chemical composition of the blood vessel wall and lesions, respectively, allowing conclusions to be drawn concerning the involvement of iNOS-derived NO in atherogenesis.

NO is vital for normal vascular function and plays an important role in vasorelaxation and in the prevention of platelet aggregation and smooth muscle cell proliferation.[65] Under normal physiological conditions, NO bioavailability is attributed to eNOS. Indeed, genetic ablation of eNOS leads to hypertension,[34] and on an atherosclerotic background, the ApoE$^{-/-}$ eNOS$^{-/-}$ mouse exhibits increased atherosclerotic lesion size.[34] In contrast, NO produced by iNOS is associated with detrimental effects. Upon induction, iNOS is capable of generating higher NO concentrations, in the micromolar range.[66] In the lesion, iNOS is induced by smooth muscle cells and inflammatory macrophages and has been shown to contribute to atherosclerotic progression, since its deletion leads to a smaller lesion size.[36–38] We have previously demonstrated that iNOS is present in lesions of aorta of Western diet-fed ApoE$^{-/-}$ mice,[49] but now demonstrate its presence in homogenized hearts from similar mice (Fig. 1). (NB: As expected, iNOS was missing in homogenized hearts of ApoE$^{-/-}$iNOS$^{-/-}$ mice.) This finding may indicate a more widespread induction of iNOS in the hearts of ApoE$^{-/-}$ mice, in addition to its presence in lesions. Indeed, we have

previously demonstrated robust protein nitration in the hearts of ApoE$^{-/-}$ mice (286.1 ± 75.0 pmol/mg protein), which is ameliorated in ApoE$^{-/-}$iNOS$^{-/-}$ mice (70.0 ± 30.7 pmol/mg protein).[49] Thus iNOS deletion reduced protein nitration in hearts of Western diet-fed ApoE$^{-/-}$ mice by 76%.[49] These combined findings are consistent with iNOS-derived NO involvement in protein nitration in the hearts of ApoE$^{-/-}$ mice.

Similarities between aortic root sections of ApoE$^{-/-}$ and ApoE$^{-/-}$iNOS$^{-/-}$ mice are revealed by micro ATR-FTIR spectroscopy

Analysis of aortic root sections from ApoE$^{-/-}$ and ApoE$^{-/-}$iNOS$^{-/-}$ mice showed similarities in the main vibrations of the vascular tissue. In this regard, the composition of the tunica media, with respect to amide I–III vibrations of the lamellae (mainly due to elastin and collagen) (Fig. 2–7), was alike in the two mouse strains. Similarities in the composition of the plaque of both strains of mice were also found in terms of the typical features associated with lipid esters, namely the ν(C=O) band at *ca.* 1733 cm^{-1} and the ν(C–O) signal at *ca.* 1170 cm^{-1}, that are consistent with cholesteryl esters (Fig. 2 and Fig. 5–7). These common features indicate that iNOS does not exert an influence on these factors. These results also indicate the reproducibility that can be afforded by this spectroscopic method. Given that different constituents characterize the tunica media and the lesion, it is possible to image these sections in a contrasting manner (Fig. 5d and 6d).

Differences between aortic root sections of ApoE$^{-/-}$ and ApoE$^{-/-}$iNOS$^{-/-}$ mice are revealed by micro ATR-FTIR spectroscopy

In some ApoE$^{-/-}$ aortic root sections, the atheroma was more bulky than that observed for the ApoE$^{-/-}$iNOS$^{-/-}$ mouse and extended into the medial layer (Fig. 6). In these bulky lesions, signals were observed due to triglycerides and free fatty acids, *i.e.* 1744 cm^{-1} and 1713 cm^{-1} due to the C=O stretching of the ester group in triglycerides (and other esterified fatty acids) and free fatty acids,[57] respectively. Some evidences of unsaturated lipids could also be observed by the presence of a minor absorption at

3005 cm^{-1} due to the olefinic $=$CH stretching of lipid acyl chains.[59]

In ApoE$^{-/-}$iNOS$^{-/-}$ mouse specimens, lesions composed of aggregates of free cholesterol were revealed through the bands at 1054 and 953 cm^{-1}, due to the C–C backbone stretching vibrations of free cholesterol (Fig. 8). Notably the spectrum of the lesion closely resembled the spectrum of pure cholesterol (Fig. 8c).

Lipid concentration is measured to be higher in aortic root sections of ApoE$^{-/-}$ mice compared to ApoE$^{-/-}$iNOS$^{-/-}$ mice by micro ATR-FTIR spectroscopy

A comparison of lipid concentrations in the intimal plaque of aortic root sections of ApoE$^{-/-}$ and ApoE$^{-/-}$iNOS$^{-/-}$ mice by micro ATR-FTIR spectroscopy indicated that lipid esters were clearly present in plaques of both ApoE$^{-/-}$ and ApoE$^{-/-}$iNOS$^{-/-}$ mice (Fig. 9), but esterified and free fatty acids were only found in lesions from ApoE$^{-/-}$ mice when small regions of plaques were analysed. A direct comparison of ATR-FTIR spectra of atherosclerotic plaques, following normalisation of both profiles to the peak intensity of the amide I band (in the 1705–1585 cm^{-1} range), also revealed that the strongest lipid bands were observed for the ApoE$^{-/-}$ mouse sample (namely C–H and ester C$=$O stretching signals) (Fig. 10). The decreased lesion size with respect to lipid content in ApoE$^{-/-}$iNOS$^{-/-}$ mice compared with ApoE$^{-/-}$ mice is consistent with quantitative data from previous findings and indicates that a lack of iNOS is beneficial with regard to lipid accumulation in the lesion.[36–38] Previous reports indicate that iNOS deletion does not affect plasma levels of cholesterol, triglycerides, glucose or nitrates in the atherosclerotic Western diet-fed ApoE$^{-/-}$ mouse,[36–38,49] albeit plasma levels of lipoperoxides were significantly reduced in the ApoE$^{-/-}$iNOS$^{-/-}$ mouse.[37,38] However, with respect to aortic cholesterol, Detmers *et al.* measured that cholesteryl esters were reduced by 57% for male ApoE$^{-/-}$iNOS$^{-/-}$ *versus* ApoE$^{-/-}$ mice at 22 weeks of age, as measured *via* an enzymatic fluorimetric method applied to the whole aorta (containing the aortic root).[36] In the current study, using micro ATR-FTIR spectroscopic images that represent a 'chemical snapshot' of a specimen at a given location, we measured the reduction in cholesteryl esters in the lesion of male ApoE$^{-/-}$iNOS$^{-/-}$ *versus* ApoE$^{-/-}$ mice at 27 weeks of age to be 63% (Fig. 9). Thus, given that it might be difficult to analyse the whole plaque by micro ATR-FTIR spectroscopic imaging, measurements concerning the relative change in the depletion of cholesteryl esters upon iNOS deletion were similar to those obtained by more conventional methods. These results indicate that in addition to using micro ATR-FTIR spectroscopic imaging as a local probe of the structural and chemical aspects of a sample, it is also possible to obtain meaningful quantitative data.

Micro ATR-FTIR spectroscopy reveals evidence of protein nitration (ordered conformation) in the lesion of ApoE$^{-/-}$ mice compared to the lesion of ApoE$^{-/-}$iNOS$^{-/-}$ mice (disordered conformation)

Further analysis of the amide I band in the spectra of the lesions revealed a change in the position of this band in the ApoE$^{-/-}$ mouse *versus* the ApoE$^{-/-}$iNOS$^{-/-}$ mouse. This shift is ascribed to a change in the secondary structure for proteins in the region of the lesion that has previously been evidenced for α-synuclein, and attributed to protein nitration.[63] For purified α-synuclein, the non-nitrated protein gave an absorption maximum in the amide I band region at 1653 cm^{-1}, indicative of a disordered conformation, whereas upon nitration, the band maximum shifted to 1625 cm^{-1}, representing a more ordered structure corresponding to β-sheet.[63] A similar effect was observed in the current study. In this regard, the ApoE$^{-/-}$iNOS$^{-/-}$ lesion gives rise to an absorption maximum at 1653 cm^{-1} (*i.e.* disordered conformation; lack of nitration) that shifted to 1632 cm^{-1} in the ApoE$^{-/-}$ lesion (*i.e.* ordered conformation), an effect attributed to protein nitration. A similar spectral shift of the amide I band indicative of a change from α-helix to β-sheet structure was also observed with conventional ATR-FTIR spectroscopy for oxidation/nitration of prion proteins.[67]

Protein nitration occurs during atherosclerosis and may contribute to necrosis and protein damage within the lesion. While the full identity of proteins nitrated during this disease may not be known, several have been characterized.[68,69] For instance, the extent of nitrated low density lipoprotein (LDL) is 90 times higher in human aortic lesions than in the plasma of healthy subjects.[41] High density lipoprotein (HDL) is also nitrated during atherosclerosis with nitrated HDL levels reportedly 6-fold higher in human atherosclerotic lesions than the circulation.[70] The nitration of both lipoproteins exerts a negative impact on the normal homeostasis of the blood vessel wall. For instance, nitrated LDL is absorbed by macrophages by the scavenger receptor pathway contributing to macrophage-driven foam cell deposition in the arterial wall.[71] Nitrated HDL is a dysfunctional form of HDL that is associated with a diminished ABCA1-dependent cholesterol efflux capacity of the lipoprotein.[72] Within murine and human atherosclerotic lesions, the enzyme cyclooxygenase (COX) is nitrated.[48,73] COX metabolizes arachidonic acid to produce prostaglandin H$_2$, a substrate for prostacyclin synthase (PGI$_2$S), an enzyme with antithrombotic, antiproliferative, and vasodilatory functions in the normal vasculature. Notably, PGI$_2$S is also nitrated and inactivated in early-stage atherosclerotic lesions.[74] Nitration of both COX and PGI$_2$S, resulting in loss of function, would therefore impact on the ability of the blood vessel to relax.

The proteins nitrated in the lesion during atherosclerosis are likely different to those nitrated in the heart. In this regard, evidence for nitration of several proteins during heart failure have been identified, that include α-actinin, sarcoplasmic reticulum Ca^{2+} ATPase (SERCA) and myofibrillar creatine kinase (MM-CK).[75–77] Notably, nitrated SERCA has also been identified in human atherosclerotic aortae.[78] These proteins are associated with normal heart function, and thus, their nitration, if associated with loss of enzyme activity, is expected to cause damage.

In summary, we have demonstrated that by micro ATR-FTIR spectroscopy, it is possible to obtain evidence consistent with protein nitration in the lesion of aortic root sections obtained from Western diet-fed ApoE$^{-/-}$ mice, which is diminished in the absence of iNOS. These data imply a role for iNOS-derived NO in changing the secondary conformation of proteins. While the identity of proteins in the lesion that are nitrated remains unknown, the main components of protein nitration are expected to be LDL and HDL.

Conclusion

Micro ATR-FTIR spectroscopic imaging was applied *ex vivo* to the atherosclerotic aortic root of ApoE$^{-/-}$ and ApoE$^{-/-}$iNOS$^{-/-}$ mice fed a high-fat Western diet. The chemical specificity and high spatial resolution of this imaging methodology enabled information about the composition and distribution of the tissue constituents to be obtained without the need of staining or labelling. Spectral analysis of the fingerprint region of the mid-IR spectrum evidenced a similar structure and chemistry of the medial lamellae in the histologies of the two animal strains, indicating no relevant involvement of the medial layer in atherogenesis. However, ApoE$^{-/-}$ and ApoE$^{-/-}$iNOS$^{-/-}$ mice aortic roots differ for the extent and biochemical composition of the intimal plaque. ApoE$^{-/-}$ mouse lesions were severely distributed across the arterial wall showing a high-fat atheroma rich in cholesteryl esters, triglycerides and free fatty acids, whereas ApoE$^{-/-}$iNOS$^{-/-}$ mouse lesions were less extended and composed of free and esterified cholesterol. The presence of iNOS in the heart of ApoE$^{-/-}$ mice was detected through the use of a specific antibody (ApoE$^{-/-}$iNOS$^{-/-}$ mice lack the gene for this enzyme). The results reported in this work demonstrate the ability of micro ATR-FTIR spectroscopic imaging to detect the chemical and structural changes occurring in the arterial wall during atherosclerosis in a murine model of the disease and quantify changes in specific constituents. This methodology may have broader implications in obtaining molecular level insight into pathological states of different tissues.

References

1 R. Ross, *Nature*, 1993, **362**, 801–809.
2 P. Libby, P. M. Ridker and A. Maseri, *Circulation*, 2002, **105**, 1135–1143.
3 F. A. Jaffer, P. Libby and R. Weissleder, *Circulation*, 2007, **116**, 1052–1061.
4 J. J. Baraga, M. S. Feld and R. P. RAVA, *Applied Spectroscopy*, 1992, **46**, 187–190.
5 J. F. Brennan III, T. J. Römer, R. S. Robert, S. Lees, A. M. Tercyak, J. Kramer, Jr. and M. S. Feld, *Circulation*, 1997, **96**, 99–105.
6 R. H. Clarke, E. B. Hanlon, J. M. Isner and H. Brody, *Applied Optics*, 1987, **26**, 3175–3177.
7 T. J. Romer, J. F. Brennan III, T. C. B. Schut, R. Wolthuis, R. C. M. van den Hoogen, J. J. Emeis, A. van der Laarse, A. V. G. Bruschke and G. J. Puppels, *Atherosclerosis*, 1998, **141**, 117–124.
8 L. P. Choo-Smith, H. G. M. Edwards, H. P. Endtz, J. M. Kros, F. Heule, H. Barr, J. S. Robinson, H. A. Bruining and G. J. Puppels, *Biopolymers*, 2002, **67**, 1–9.
9 C. W. Freudiger, W. Min, B. G. Saar, S. Lu, G. R. Holtom, C. He, J. C. Tsai, J. X. Kang and S. Xie, *Science*, 2008, **322**, 1857–1861.
10 M. Jackson, M. G. Sowa and H. H. Mantsch, *Biophysical Chemistry*, 1997, **68**, 109–125.
11 D. R. Kodali, D. M. Small, J. Powell and K. Krishnan, *Applied Spectroscopy*, 1991, **45**, 1310–1317.
12 D. J. Moore, C. R. Flach, R. Mendelsohn and G. Zhang, *Journal of Investigative Dermatology*, 2007, **127**, 502.
13 H. Ou-Yang, E. P. Paschalis, A. L. Boskey and R. Mendelsohn, *Applied Spectroscopy*, 2002, **56**, 419–422.
14 C. Krafft, L. Shapoval, S. B. Sobottka, K. D. Geiger, G. Schackert and R. Salzer, *Biochimica Et Biophysica Acta-Biomembranes*, 2006, **1758**, 883–891.
15 R. Salzer, G. Steiner, H. H. Mantsch, J. Mansfield and E. N. Lewis, *Fresenius Journal of Analytical Chemistry*, 2000, **366**, 712–726.
16 K. Wehbe, R. Pinneau, M. Moenner, G. Deleris and C. Petibois, *Analytical and Bioanalytical Chemistry*, 2008, **392**, 129–135.
17 F. Bonnier, D. Bertrand, S. Rubin, L. Venteo, M. Pluot, B. Baehrel, M. Manfait and G. D. Sockalingum, *Analyst*, 2008, **133**, 784–790.
18 F. Bonnier, S. Rubin, L. Venteo, C. M. Krishna, M. Pluot, B. Baehrel, M. Manfait and G. D. Sockalingum, *Biochimica Et Biophysica Acta-Biomembranes*, 2006, **1758**, 968–973.
19 C. Petibois and G. Deleris, *Trends in Biotechnology*, 2006, **24**, 455–462.
20 K. R. Bambery, E. Schultke, B. R. Wood, S. T. R. MacDonald, K. Ataelmannan, R. W. Griebel, B. H. J. Juurlink and D. McNaughton, *Biochimica Et Biophysica Acta-Biomembranes*, 2006, **1758**, 900–907.
21 Y.-H. Hwang, J. Cho, F. Tay, J. Y. Y. Heng, R. Ho, S. G. Kazarian, D. R. Williams, A. R. Boccaccini, J. M. Polak and A. Mantalaris, *Biomaterials*, 2009, **30**, 499–507.
22 J. Lee, E. Gazi, J. Dwyer, M. D. Brown, N. W. Clarke, J. M. Nicholson and P. Gardner, *Analyst*, 2007, **132**, 750–755.
23 M. K. Kuimova, K. L. A. Chan and S. G. Kazarian, *Applied Spectroscopy*, 2009, **63**, 164–171.
24 L. Wang, J. Chapman, R. A. Palmer, O. van Ramm and B. Mizaikoff, *Journal of Biomedical Optics*, 2007, **12**, 024006.
25 L. Q. Wang, J. Chapman, R. A. Palmer, T. M. Alter, B. A. Hooper, O. van Ramm and B. Mizaikoff, *Applied Spectroscopy*, 2006, **60**, 1121–1126.
26 C. S. Colley, S. G. Kazarian, P. D. Weinberg and M. J. Lever, *Biopolymers*, 2004, **74**, 328–335.
27 S. G. Kazarian and K. L. A. Chan, *Biochimica Et Biophysica Acta-Biomembranes*, 2006, **1758**, 858–867.
28 F. Palombo, S. G. Cremers, P. D. Weinberg and S. G. Kazarian, *Journal of Royal Society Interface*, 2008, DOI: 10.1098/rsif.2008.0325.
29 D. J. Stuehr, *Annu Rev Pharmacol Toxicol*, 1997, **37**, 339–359.
30 Y. Xia and J. L. Zweier, *Proc Natl Acad Sci U S A*, 1997, **94**, 6954–6958.
31 Y. Xia, A. L. Tsai, V. Berka and J. L. Zweier, *J Biol Chem*, 1998, **273**, 25804–25808.
32 S. Pou, L. Keaton, W. Surichamorn and G. M. Rosen, *J Biol Chem*, 1999, **274**, 9573–9580.
33 J. N. Wilcox, R. R. Subramanian, C. L. Sundell, W. R. Tracey, J. S. Pollock, D. G. Harrison and P. A. Marsden, *Arterioscler. Thromb. Vasc. Biol.*, 1997, **17**, 2479–2488.
34 J. W. Knowles, R. L. Reddick, J. C. Jennette, E. G. Shesely, O. Smithies and N. Maeda, *J. Clin. Invest.*, 2000, **105**, 451–458.
35 S. Hoetten, H. Kai, J. Widder, G. Riehl, A. Marx, P. L. Huang, G. Ertl and P. J. Kuhlencordt, *Circulation*, 2003, **108**, 40–40.
36 P. A. Detmers, M. Hernandez, J. Mudgett, H. Hassing, C. Burton, S. Mundt, S. Chun, D. Fletcher, D. J. Card, J. Lisnock, R. Weikel, J. D. Bergstrom, D. E. Shevell, A. Hermanowski-Vosatka, C. P. Sparrow, Y. S. Chao, D. J. Rader, S. D. Wright and E. Pure, *Journal of Immunology*, 2000, **165**, 3430–3435.
37 P. J. Kuhlencordt, J. Chen, F. Han, J. Astern and P. L. Huang, *Circulation*, 2001, **103**, 3099–3104.
38 T. Miyoshi, Y. H. Li, D. M. Shih, X. P. Wang, V. E. Laubach, A. H. Matsumoto, G. A. Helm, A. J. Lusis and W. B. Shi, *Life Sciences*, 2006, **79**, 525–531.
39 A. A. Quyyumi, N. Dakak, N. P. Andrews, S. Husain, S. Arora, D. M. Gilligan, J. A. Panza and R. O. Cannon, *Journal of Clinical Investigation*, 1995, **95**, 1747–1755.
40 L. D. Buttery, D. R. Springall, A. H. Chester, T. J. Evans, E. N. Standfield, D. V. Parums, M. H. Yacoub and J. M. Polak, *Lab Invest*, 1996, **75**, 77–85.
41 C. Leeuwenburgh, M. M. Hardy, S. L. Hazen, P. Wagner, S. Oh-ishi, U. P. Steinbrecher and J. W. Heinecke, *J Biol Chem*, 1997, **272**, 1433–1436.

42 C. S. Baker, R. J. Hall, T. J. Evans, A. Pomerance, J. Maclouf, C. Creminon, M. H. Yacoub and J. M. Polak, *Arterioscler Thromb Vasc Biol*, 1999, **19**, 646–655.

43 J. S. Luoma, P. Stralin, S. L. Marklund, T. P. Hiltunen, T. Sarkioja and S. Yla-Herttuala, *Arterioscler Thromb Vasc Biol*, 1998, **18**, 157–167.

44 J. S. Beckmann, Y. Z. Ye, P. G. Anderson, J. Chen, M. A. Accavitti, M. M. Tarpey and C. R. White, *Biol Chem Hoppe Seyler*, 1994, **375**, 81–88.

45 S. H. Zhang, R. L. Reddick, J. A. Piedrahita and N. Maeda, *Science*, 1992, **258**, 468–471.

46 R. W. Mahley, *Science*, 1988, **240**, 622–630.

47 J. L. Breslow, *Science*, 1996, **272**, 685–688.

48 R. S. Deeb, H. Shen, C. Gamss, T. Gavrilova, B. D. Summers, R. Kraemer, G. Hao, S. S. Gross, M. Laine, N. Maeda, D. P. Hajjar and R. K. Upmacis, *American Journal of Pathology*, 2006, **168**, 349–362.

49 R. K. Upmacis, M. J. Crabtree, R. S. Deeb, H. Shen, P. B. Lane, L. E. S. Benguigui, N. Maeda, D. P. Hajjar and S. S. Gross, *American Journal of Physiology-Heart and Circulatory Physiology*, 2007, **293**, H2878–H2887.

50 F. Wu, J. X. Wilson and K. Tyml, *American Journal of Physiology-Regulatory Integrative and Comparative Physiology*, 2003, **285**, R50–R56.

51 J. A. Scott, M. L. Weir, S. M. Wilson, J. W. Xuan, A. F. Chambers and D. G. McCormack, *American Journal of Physiology-Heart and Circulatory Physiology*, 1998, **44**, H2258–H2265.

52 D. Steinberg, S. Parthasarathy, T. E. Carew, J. C. Khoo and J. L. Witztum, *New England Journal of Medicine*, 1989, **320**, 915–924.

53 F. S. Parker, *Applied Spectroscopy*, 1975, **29**, 129–147.

54 M. K. Ahmed, J. Daun and D. DeClercq, *Applied Spectroscopy*, 1998, **52**, 990–993.

55 J. M. Clark and S. Glagov, *Arteriosclerosis*, 1985, **5**, 19–34.

56 H. Wolinsky and S. Glagov, *Circulation Research*, 1964, **14**, 400–413.

57 A. A. Ismail, F. R. Vandevoort, G. Emo and J. Sedman, *Journal of the American Oil Chemists Society*, 1993, **70**, 335–341.

58 S. Yoshida, Y. Okazaki, T. Yamashita, H. Ueda, R. Ghadimi, A. Hosono, T. Tanaka, K. Kuriki, S. Suzuki and S. Tokudome, *Lipids*, 2008, **43**, 361–372.

59 F. Severcan, G. Gorgulu, S. T. Gorgulu and T. Guray, *Analytical Biochemistry*, 2005, **339**, 36–40.

60 O. Kleiner, J. Ramesh, M. Huleihel, B. Cohen, K. Kantarovich, C. Levi, B. Polyak, R. S. Marks, J. Mordehai, Z. Cohen and S. Mordechai, *BMC Gastroenterol*, 2002, **2**, 1–14.

61 M. M. Paradkar and J. Irudayaraj, *International Journal of Dairy Technology*, 2002, **55**, 127–132.

62 P. Tandon, G. Forster, R. Neubert and S. Wartewig, *Journal of Molecular Structure*, 2000, **524**, 201–215.

63 V. N. Uversky, G. Yamin, L. A. Munishkina, M. A. Karymov, I. S. Millett, S. Doniach, Y. L. Lyubchenko and A. L. Fink, *Molecular Brain Research*, 2005, **134**, 84–102.

64 P. I. Haris, in *Infrared Analysis of Peptides and Proteins: Principles and Applications*, ed. B. R. Singh, American Chemical Society, Washington, DC, 1999, pp. 54–95.

65 M. W. Radomski and E. Salas, *Atherosclerosis*, 1995, **118**, S69–S80.

66 J. MacMicking, Q. W. Xie and C. Nathan, *Annu. Rev. Immunol.*, 1997, **15**, 230–350.

67 D. V. Dear, D. S. Young, J. Kazlauskaite, F. Meersman, D. Oxley, J. Webster, T. J. T. Pinheiro, A. C. Gill, I. Bronstein and C. R. Lowe, *Biochimica et Biophysica Acta*, 2007, **1774**, 792–802.

68 G. Peluffo and R. Radi, *Cardiovascular Research*, 2007, **75**, 291–302.

69 R. K. Upmacis, *Lipid Insights*, 2008, **2**, 75–88.

70 S. Pennathur, C. Bergt, B. H. Shao, J. Byun, S. Y. Kassim, P. Singh, P. S. Green, T. O. McDonald, J. Brunzell, A. Chait, J. F. Oram, K. O'Brien, R. L. Geary and J. W. Heinecke, *Journal of Biological Chemistry*, 2004, **279**, 42977–42983.

71 A. Graham, N. Hogg, B. Kalyanaraman, V. O'Leary, V. Darley-Usmar and S. Moncada, *FEBS Lett*, 1993, **330**, 181–185.

72 L. M. Zheng, B. Nukuna, M. L. Brennan, M. J. Sun, M. Goormastic, M. Settle, D. Schmitt, X. M. Fu, L. Thomson, P. L. Fox, H. Ischiropoulos, J. D. Smith, M. Kinter and S. L. Hazen, *Journal of Clinical Investigation*, 2004, **114**, 529–541.

73 R. S. Deeb, M. J. Resnick, D. Mittar, T. McCaffrey, D. P. Hajjar and R. K. Upmacis, *J Lipid Res*, 2002, **43**, 1718–1726.

74 M. H. Zou, M. Leist and V. Ullrich, *Am J Pathol*, 1999, **154**, 1359–1365.

75 A. Borbely, A. Toth, I. Edes, L. Virag, J. G. Papp, A. Varro, W. J. Paulus, J. van der Velden, G. J. M. Stienen and Z. Papp, *Cardiovascular Research*, 2005, **67**, 225–233.

76 A. J. Lokuta, N. A. Maertz, S. V. Meethal, K. T. Potter, T. J. Kamp, H. H. Valdivia and R. A. Haworth, *Circulation*, 2005, **111**, 988–995.

77 M. J. Mihm, C. M. Coyle, B. L. Schanbacher, D. M. Weinstein and J. A. Bauer, *Cardiovascular Research*, 2001, **49**, 798–807.

78 T. Adachi, R. Matsui, S. Q. Xu, M. Kirber, H. L. Lazar, V. S. Sharov, C. Schoneich and R. A. Cohen, *Circulation Research*, 2002, **90**, 1114–1121.